Dynamic Adsorption of CO 2 by CHA Zeolites -Size Matters

Edwin Clatworthy, Sajjad Ghojavand, Rémy Guillet-Nicolas, Jean-Pierre Gilson, Philip Llewellyn, Nikolai Nesterenko, Svetlana Mintova

Dynamic Adsorption of CO_2 by CHA Zeolites – Size Matters

Edwin B. Clatworthy,[†] Sajjad Ghojavand,[†], Rémy Guillet-Nicolas,[†] Jean-Pierre Gilson,[†] Philip L. Llewellyn,[‡] Nikolai Nesterenko,[‖] Svetlana Mintova[†]**

† Normandie Université, ENSICAEN, UNICAEN, CNRS, Laboratoire Catalyse et Spectrochimie (LCS), 14050 Caen, France

‡ TotalEnergies OneTech, Centre Scientifique et Technique Jean Féger, Pau, France

‖ TotalEnergies OneTech Belgium, Feluy, B-7181 Seneffe, Belgium

ABSTRACT The performance of K-CHA nanozeolite composed of discrete nanoparticles prepared by an organic template-free direct synthesis is compared to that of conventional micron-sized K-CHA with an order of magnitude difference in particle size and identical chemical composition (Si/Al ratio and cations) for the separation of dilute CO_2 from N_2. Breakthrough curve analysis of the zeolites meshed to identical sizes demonstrates the superior performance of nanozeolites for gas separation due to the significantly faster diffusion of CO_2 molecules through the bed composed of meshed nanozeolite particles evidenced by the enhanced mass transfer, more rapid establishment of equilibrium, and faster desorption of CO_2. Modelling of the CO_2 breakthrough curves indicates enhanced mass transfer properties of the CHA nanozeolite due to the higher linear driving force parameter values. Variation of the modelling parameters and back-calculation of the diffusion coefficients indicates that axial diffusion contributes significantly to the mass transfer behaviour yet also reveals significantly lower micropore diffusion resistance for the nano-sized K-CHA. These results demonstrate for rapid kinetically controlled sorption-based

separations, that by reducing the size of the discrete crystallites of the meshed adsorbent particle by an order of magnitude, significant improvements in the utilization of the bed can be achieved due to the shortening of the mass-transfer zone, improving the separation performance.

Keywords: zeolites, crystal size, CO_2 adsorption, separation, breakthrough analysis

Nomenclature

c_{in}	concentration at column inlet, mol·m^{-3}
c_{out}	concentration at column outlet, mol·m^{-3}
$c_{g,i}$	component concentration in the gas phase, mol·kg^{-1}
c_{pg}	specific heat capacity of gas at constant pressure, J·kg^{-1}·K^{-1}
c_{ps}	specific heat capacity of adsorbent at constant pressure, J·kg^{-1}·K^{-1}
c_{pw}	specific heat capacity of wall at constant pressure, J·kg^{-1}·K^{-1}
D_{ax}	axial mass dispersion coefficient, m^2·s^{-1}
D_c	micropore diffusivity, m^2·s^{-1}
D_p	macropore diffusivity, m^2·s^{-1}
d_i	internal diameter of column, m
K	dimensionless Henry's Law equilibrium constant
K_i	affinity constant
$K_{i,0}$	affinity constant at reference temperature
k_f	film mass transfer coefficient, s^{-1}
k_i	overall mass transfer coefficient, s^{-1}
k_{in}	heat transfer coefficient between the bed and wall, W·m^{-2}·K^{-1}
k_{out}	heat transfer coefficient between the wall and bath, W·m^{-2}·K^{-1}
k_{LDF}	effective mass transfer coefficient, s^{-1}
$n_{adsorbed}$	amount of molecules adsorbed, mol
q_{eq}	adsorbed concentration in equilibrium with $c_{g,i}$, mol·kg^{-1}
$\overline{q_i}$	component average concentration on the adsorbed phase, mol·kg^{-1}
$q_{max,i}$	maximal loading, mol·kg^{-1}
$q_{max0,i}$	maximal loading at reference temperature T_0, mol·kg^{-1}
R	ideal gas constant, J·mol^{-1}·K^{-1}
r_c	average crystal radius, m
r_p	average particle radius, m
T	bulk phase temperature, K
T_0	reference temperature for isotherm fitting
T_w	wall temperature, K
T_{env}	environmental temperature (reference temperature), K
t	Toth heterogeneity parameter
t_0	heterogeneity parameter at reference temperature T_0
u	interstitial velocity, m·s^{-1}
V_{He}	volume of He, m^{-3}

V_{in}	volume at column inlet, m^{-3}
V_{out}	volume at column outlet, m^{-3}
WS	wall thickness, m
$y_{adsorptive,i}$	adsorptive volume fraction
ΔH_{ads}	isosteric enthalpy of adsorption, $J \cdot mol^{-1}$
ΔH_i	isosteric enthalpy of adsorption for component i, $J \cdot mol^{-1}$
α	parameter for the temperature dependency of the Toth exponent
ε	bed porosity
ε_p	particle porosity
λ	axial heat dispersion coefficient, $J \cdot s^{-1} \cdot m^{-1} \cdot K^{-1}$
ρ_p	average particle density, $kg \cdot m^{-3}$
ρ_b	average fixed bed density, $kg \cdot m^{-3}$
ρ_g	fluid density, $kg \cdot m^{-3}$
ρ_w	wall density, $kg \cdot m^{-3}$
χ_i	coefficient for the temperature dependency of the maximum capacity

Introduction

The bulk separation and purification of gases are essential industrial processes in which zeolites play key roles in a range of applications including gas drying, S removal, O_2 and N_2 production, landfill gas separation (CO_2/CH_4), and H_2 production from methane reforming and refinery off-gas.[1] In the last decade enormous efforts have been dedicated to developing materials for carbon capture and storage (CCS) because of the rising atmospheric concentration of CO_2 and its contribution to anthropogenic global climate change.[2-22] However, due to the presence of H_2O in industrial streams, such as flue gas, the energy and cost efficient separation of CO_2 is considerably challenging. The high cationic content of industrial molecular sieves, such as 4A, 5A and 13X, and their strong interaction with H_2O demands appropriate regeneration to maintain their longevity. Employment of activated alumina upstream of the molecular sieve can be also increase their lifetime considerably, but at additional capital cost.[23] While solvent-based absorption processes are currently the most widely applied for post-combustion CO_2 capture, these can be associated with large energy requirements for regeneration, degradation issues with temperature and the presence

of oxygen and toxicity.[24-26] With these points in mind, alternatives to the use of amines solvents such as green solvents, membranes and adsorption-based separations are investigated, with the latter of interest to the current study. Pressure swing adsorption (PSA) and temperature swing adsorption (TSA) are the processes often used for gas separation. Whilst PSA processes can be quite rapid (steps can occur in seconds), currently mature TSA process cycles can be quite long (hours). Whilst TSA may be quite adapted to anthropogenic CO_2 capture, shorter process sequences are required. A rapid TSA process is currently being developed,[27] where the whole capture, regeneration and conditioning steps can take a minute. In such cases however, kinetics of the gas/solid interactions are as important as the thermodynamics and to control the gas diffusion at the particle level can prove critical to separation properties.

The development of zeolite materials possessing high CO_2 separation performance has been a focal point because of the established roles zeolites play in petrochemistry and air separation processes thereby providing a rapidly deployable solution at an industrial scale.[23, 28] However, conventional zeolites are composed of micrometre sized particles which means a CO_2 molecule must diffuse a distance through the pores of a particle tens of thousands of times longer than its size. This problem can be partly addressed by improving molecular access to the zeolite micropores through introducing mesoporosity, or by reducing the particle size.[29, 30] However, while creating mesoporosity can significantly improve the diffusion and catalytic properties of zeolites, it typically involves either post-synthesis treatments or the use of expensive organic templates and structure directing agents, increasing the time, cost and waste of the material production.[31]

By preparing zeolites with nanoscale dimensions the distance guest molecules must diffuse through the particle can be reduced by an order of magnitude. To benefit from this we have developed pure inorganic one-pot syntheses of industrially important nanozeolites composed

of discrete nanoparticles.[32-38] While the yield of particular nanozeolite syntheses warrants further optimisation, the elimination of expensive organic structure-directing agents (OSDAs) and calcination treatments offers a reduction in energy consumption and emissions while also avoiding undesirable changes to the zeolite structure and properties caused by H_2O vapour during calcination. Here we report on the comparison of K-CHA zeolites for the separation of CO_2 from a dilute stream at various temperatures, investigating the difference in performance by varying only the size of the discrete zeolite particles forming the meshed particles by an order of magnitude; the size of the meshed particles for both samples is identical. We provide direct experimental evidence and validation of the enhanced diffusion properties of adsorbent particles composed of discrete nano-sized zeolites applicable to industrially relevant separations. The concentration of CO_2 employed (5 vol%) is comparable to that of the exhaust of a natural gas combined-cycle plant.[39] The choice of examining high aluminium (Si/Al < 3) K-CHA zeolite derives from their attractive properties for CO_2 separation applications, *i.e.*, high CO_2 capacity, and selectivity towards CO_2 over N_2 (4 mmol/g, 27 with Si/Al = 2.4 and 2.1 mmol/g, 80 with Si/Al = 1.2).[6, 40, 41]

Experimental

Materials

All reagents were used as received unless otherwise specified. Potassium hydroxide (90 wt%), LUDOX AS-40, sodium aluminate ($NaAlO_2$, 40–45% Na_2O, 50–56% Al_2O_3) and sodium hydroxide pellets (98 wt%) were purchased from Sigma-Aldrich. An aqueous solution of caesium hydroxide (CsOH, 50 wt% Cs) was prepared by dissolving caesium hydroxide (Alfa Aesar 20% H_2O, 98%) in ultrapure (Type 1) water. Zeolite Y (H-form, CBV400), was purchased from Zeolyst. Ultrapure water was prepared by a Milli-Q Direct 8 system and used for all syntheses. Quartz fine granular washed and calcined (900 °C, 0.2–0.8

mm, Merck) was used for blank breakthrough curve measurements. Helium (helium 4.5, ≥ 99.995%), carbon dioxide (dioxyde de carbone 4.5, ≥ 99.995%) and nitrogen (azote 5.0, ≥ 99.999%) were purchased from Linde.

Synthesis

Micron-sized K-CHA was prepared according to the procedure employed by Shang *et al*.[40] Zeolite Y powder (CBV400, 25 g) was added to de-ionised water (198 mL) and 9.5 M KOH solution (27 mL) in a sealed 250 mL polypropylene bottle. The mixture was shaken for 30 s and then placed in an oven preheated at 95 °C for 15 days. The sample was then cooled to room temperature and washed with de-ionised water by centrifugation at 20,000 rpm until the supernatant had a pH value between 7 and 8. The washed sample was then oven-dried at 60 °C overnight. The yield of the micron-sized K-CHA based on the initial mass of CBV400 was 37%.

Nano-sized K-CHA was prepared according to a procedure described previously.[42] 10.8 g of $NaAlO_2$ was mixed with 84.0 g of water with rapid stirring. Afterwards, 34.3 g of NaOH, 16.5 g of KOH, and 8.8 g of CsOH (50 wt% Cs in water) were added and stirred for 2 h to obtain a clear solution. 200 g of LUDOX AS-40 was added dropwise under vigorous stirring to make a final composition of 0.284 Cs_2O: 2.27 K_2O: 8.56 Na_2O: 22.9 SiO_2: 1.00 Al_2O_3: 198 H_2O. The alkali colloidal gel was then aged under vigorous stirring at room temperature for 17 days followed by hydrothermal treatment in a static oven at 90 °C for 7 h. The CHA nanocrystals were recovered by centrifugation and washed with hot water (90 °C) until a neutral pH (7–8) of the decanted solution was achieved. The recovered CHA nanocrystals were dried in an oven at 60 °C overnight. The final as-prepared CHA nanocrystals were ion exchanged with a 1 M KCl solution with a liquid/solid ratio (ml/g) of 40 for 2 hours. Afterwards, the CHA nanocrystals were recovered by centrifugation and washed with

deionised water three times. This procedure was repeated three times, and the recovered nano-sized K-CHA was dried in an oven at 60 °C overnight. The yield of the nano-sized K-CHA based on the initial combined mass of SiO_2 and Al_2O_3 was 21%.

Characterisation

Powder X-ray diffraction (PXRD) patterns were collected with a PANalytical X'Pert Pro diffractometer using Cu-Kα_1 radiation (λ = 1.5406 Å, 45 kV, 40 mA). The patterns were collected between 5 and 60° 2θ with a step size of ~0.0167° and time per step of 1000 s. Elemental analysis was performed by inductively-coupled plasma mass spectrometry (ICP-MS) using a 7900 ICP-MS from Agilent Technologies. Samples (50 mg) were digested at 110 °C for 1 h with hydrofluoric acid and aqua regia (6:1 vol. ratio) followed by neutralisation with boric acid (2 g) and de-ionised water (10 mL) and stirred overnight. The samples were then diluted up to 100 mL; a 10 mL aliquot was filtered before analysis. Thermogravimetric analysis (TG/DTG) was performed using a Setsys Evolution (SETARAM). Analysis under air was performed by heating from 30 to 800 °C (heating rate of 10 °C min^{-1}) and held at 800 °C for 10 minutes. Scanning electron microscopy (SEM) of samples was performed using a Tescan Mira I LMH operating at 30 kV, samples were coated in metal before analysis. Particle size analysis was performed using ImageJ. Energy-dispersive X-ray spectroscopy (EDS) analysis of samples was performed using two Bruker XFLASH 6/30 detectors; the composition was determined from the average of several different measured points. Low temperature N_2 adsorption/desorption isotherms were measured at −196 °C using a Micromeritics 3Flex Surface Characterization unit. Samples were degassed at 350 °C (heating rate of 1 °C min^{-1}) under vacuum for 8 h prior to analysis. High temperature (20, 40 and 60 °C) N_2 and CO_2 adsorption isotherms were measured on a Micromeritics ASAP 2020 instrument, samples were degassed at 350 °C (heating rate of 1 °C min^{-1}) under vacuum for 8 h. CO_2 and N_2 isosteric enthalpies of adsorption (ΔH_{ads}) were

calculated directly from the experimental data points of the isotherms recorded at 20, 40 and 60 °C using the Clausius Clapeyron equation in the VersaWin software. Mercury porosimetry was performed using a Micromeritics AutoPore V. *In situ* FTIR spectroscopic analysis was performed using a self-supported pellet (~20 mg, 16 mm diameter) of zeolite sample; the transmission spectra were recorded with a ThermoScientific Nicolet iS50 FTIR spectrometer equipped with an MCT detector, at a spectral resolution of 4 cm^{-1}. An IR-cell equipped with a heating device was used to activate the samples at 350 °C prior to the measurements. The cell was connected to a high vacuum line of 10^{-6} Torr. The sample was activated by heating with a ramp rate of 3 °C min^{-1} followed by heating at 350 °C for 4 h under high vacuum. All spectra were recorded at room temperature and normalised to the area and mass of the pellet; determination of the physisorption and chemisorption isotherms was performed as described previously.[43]

Breakthrough Curve Analysis

Breakthrough curve experiments were performed using a 3P Instruments mixSorb SHP eco and Cirrus-3 Quadrupole Mass Spectrometer. Powder samples of zeolite adsorbent were initially pelletised by loading the powder between two core dice in a 20 mm die sleeve, with a base plate and plunger, and increasing the applied pressure to ~1.5 tonnes. The pellets were gently crushed with an agate pestle and meshed from 60 to 35 (250–500 μm) before being loaded into the column, weighed, and covered with a thin layer of glass wool. After each instance of loading the meshed sample into the column, the column was tapped 100 times to remove inter-particle voids. The inner diameter of the column was 6 mm and the height of the adsorbent bed was 6 cm. The ratio of the column inner diameter to the meshed particle diameter was 12−24. The samples were pre-treated under He flow (20 mL/min) with heating from room temperature to 300 °C at 10 °C/min (measured by an internal temperature probe) and held at 300 °C for 6 h using a heating mantle. TG analysis of the zeolite samples was

performed to determine the weight-loss of water during the pre-treatment step. The final amounts of nano-sized and micron-sized K-CHA loaded in the column after activation were 0.601 and 0.676 g respectively. After pre-treatment the samples were kept under a flow of He (20 mL) at room temperature before commencing the breakthrough curve experiments.

Breakthrough curve experiments were conducted using a ternary mixture of CO_2, N_2 (analytical components) and He (carrier gas) at 1 bar with a flowrate of 2, 10 and 28 mL/min respectively (total 40 mL/min), representing 5, 25 and 70 vol% of the feed composition for the adsorption step. Prior to the breakthrough curve experiments the mass spectrometer was calibrated by passing the ternary feed mixture through a bypass line to the mass spectrometer. Before contacting the ternary feed mixture with the adsorbent column the sample was maintained under He flow. The adsorption feed mixture was flowed through the adsorbent column after the temperature and spectrometer signals were stable, as determined using a bypass line. After a specified amount of time whereby the bed had reached equilibrium, desorption was conducted immediately by switching the feed to 100% He (40 mL/min). Both the adsorption and desorption steps for each experiment were conducted at the same temperature; experiments were conducted at 20, 40 and 60 °C by immersing the column in a water bath isothermally maintained by a chiller. The time for each step of the analysis was 60 min at 20 °C and 30 min at 40 and 60 °C to allow sufficient time for the bed to reach equilibrium after breakthrough. The pressure drop across the column loaded with sample was determined by a pressure sensor located immediately before the column and the pressure controller located immediately after the column. For all experiments conducted the pressure drop was < 0.07 bar or 6% of the column pressure.

All breakthrough curve data was processed using the mixSorb Manager software. The differential loading of the adsorbates (CO_2 and N_2) was calculated from the integrated areas exemplified in Figures S1 and S2.

$$n_{\text{adsorbed}} = \int V_{\text{in}}(t)c_{\text{in}}(t)dt - \int V_{\text{out}}(t)c_{\text{out}}(t)dt \quad (1)$$

The advanced computed flowrate changes was employed to account for changes in the flow rate using the He carrier gas as an internal standard.

$$V_{\text{out}}(t) = \frac{V_{\text{He}}(t)}{1-\sum_{i=1}^{n} y_{\text{adsorptive},i}(t)} \quad (2)$$

Blank experiments under identical feed composition, temperature, flowrate and pressure conditions were performed using granular quartz to determine the loading of molecules in the free space between the adsorbent particles and were directly subtracted from the loading values of the zeolite samples (Fig. S3). He is considered as a non-adsorbing gas. The dead-time of the system was estimated at ≈2 s based on the time of the activation of the mass-flow controllers and the recording of the flow composition by the mass spectrometer through the by-pass line. The void fraction or bed porosity was calculated using the dry mass of the meshed K-CHA zeolite, the bulk particle density, and the internal column volume.

Breakthrough Curve Modelling

All isotherm and CO_2 breakthrough curve modelling was performed using the 3P-Sim software package. The experimental CO_2 adsorption isotherms were fitted with a temperature dependent model. Sips, Dual-Site Langmuir and Toth models were employed; Toth afforded the best goodness of fit of the data and was employed for the CO_2 breakthrough curve modelling. The parameters obtained from the modelling of the CO_2 adsorption isotherms with the Toth equation (3) which were used in the CO_2 breakthrough curve modelling are presented in Table S4.

$$q_{eq} = q_{max,i} \cdot \frac{K_i \cdot c_{g,i}}{(1+(K_i \cdot c_{g,i})^t)^{\frac{1}{t}}} \quad (3)$$

The temperature dependency of the isotherm parameters including the affinity constant, K_i, maximum loading, q_{max}, and heterogeneity parameter, t, are accounted for with the following equations:

$$K_i = K_0 \cdot exp\left(\frac{\Delta H_{ads}}{R}\left(\frac{1}{T} - \frac{1}{T_0}\right)\right) \quad (4)$$

$$q_{max,i} = q_{max,0} \cdot exp\left(\chi_i\left(1 - \frac{T}{T_0}\right)\right) \quad (5)$$

$$t = t_0 + \alpha\left(1 - \frac{T}{T_0}\right) \quad (6)$$

Global parameters for the CO_2 breakthrough curve modelling are presented in Table 1. Breakthrough curves were calculated with the following assumptions commonly employed in the literature:[44, 45]

1. Ideal gas behaviour of the adsorptive through the column.
2. No mass, heat or velocity gradients in the radial direction; instantaneous thermal equilibrium between the adsorbent and gas.
3. Dispersed plug flow model.
4. Negligible effects due to external mass transfer (film mass transfer and macropore diffusion).
5. Description of the mass transfer through the particle by the linear driving force (LDF) model.[46-48]
6. Heat capacity of the carrier gas dominates.
7. Heat capacity of the adsorbed phase neglected.
8. Constant internal (bed-wall) and external (wall-bath) heat transfer, and axial heat dispersion.
9. Constant and uniform adsorbent/bed porosity.

10. No pressure drop, constant pressure.

The model consists of dispersive plug flow with non-isothermal behaviour and variable gas velocity described by a mass and energy balance for the fixed bed and an energy balance for the column wall. The mass balance is expressed as:

$$\frac{\partial c_{g,i}}{\partial t} = D_{ax}\frac{\partial^2 c_{g,i}}{\partial z^2} - u\frac{\partial c_{g,i}}{\partial z} - c_{g,i}\frac{\partial u}{\partial z} - \frac{(1-\varepsilon)}{\varepsilon}\rho_p\frac{\partial \bar{q}_i}{\partial t} \quad (7)$$

With respect to the assumptions employed for the calculations, the two energy balance equations are expressed as:

$$\Delta H_i \rho_b (1-\varepsilon)\frac{\partial \bar{q}_i}{\partial t} - \left(c_{ps}\cdot\rho_b(1-\varepsilon) + c_{pg}\cdot\varepsilon\cdot\rho_g\right)\frac{\partial T}{\partial t} - u\varepsilon\rho_g c_{pg}\frac{\partial T}{\partial z} - T\varepsilon\rho_g c_{pg}\frac{\partial u}{\partial z} +$$

$$\lambda\varepsilon\frac{\partial^2 T}{\partial z^2} - k_{in}\frac{4}{d_i}(T - T_w) = 0 \quad (8)$$

$$k_{in}\cdot d_i(T - T_w) - (d_i\cdot WS + WS^2)c_{pw}\cdot\rho_w\frac{\partial T_w}{\partial t} - k_{out}(d_i + 2\cdot WS)(T_w - T_{env}) = 0 \quad (9)$$

The heat transfer parameters, k_{in} (bed-wall) and k_{out} (wall-bath), and the axial heat dispersion (λ) were estimated according to the according to the shape of the breakthrough curve. The axial dispersion coefficient was calculated using the correlation according to Kast in the 3P-Sim software package [47]:

$$D_{ax} = u\cdot\frac{3\cdot10^{-3}}{2} \text{ for } 2r_p < 3 \text{ mm} \quad (10)$$

Neglecting the external mass transfer resistance and using the LDF approach, the mass transfer is expressed as[49]:

$$\frac{\partial \bar{q}_i}{\partial t} = k_{LDF}(q_{eq} - \bar{q}_i) \quad (11)$$

The LDF parameter was assumed to be constant for a given operation and fitted to each breakthrough curve. Calculations were performed using the Crank-Nicolson solver (trapezoid

scheme). The bed porosity was calculated from the dry mass of zeolite and the bulk particle density.

Table 1. Column, adsorbent and carrier gas parameters used for modelling the CO_2 breakthrough curves of the nano- and micron-sized K-CHA.

Parameter	**Value**		**Source**
Column			
Bed height (cm)	6		Measured
Column inner diameter (cm)	0.6		Manufacturer
Gas flow ($mL \cdot min^{-1}$)	40		Measured
Column temperature (°C)	20, 40, 60		Measured
Pressure (bar)	1.1		Measured
Axial dispersion coefficient ($m^2 \cdot s^{-1}$)	nano	micron	W. Kast estimation
	8.98×10^{-5}	6.97×10^{-5}	
	9.46×10^{-5}	7.40×10^{-5}	
	9.89×10^{-5}	7.92×10^{-5}	
Wall thickness (mm)	3		Manufacturer
Wall density ($g \cdot cm^{-3}$)	7.9		Assumed, stainless steel
Heat transfer bed-wall (internal), [$W/(m^2 \cdot K)$]	50		Estimated
Heat transfer wall-bath (external), [$W/(m^2 \cdot K)$]	500		Estimated
Heat capacity wall [$J/(K \cdot g)$]	0.477		Assumed, stainless steel
Axial heat dispersion [$J/(K \cdot min \cdot cm)$]	5		Estimated
Adsorbent			
Mass (g)	0.601 (nano), 0.676 (micron)		Measured
Particle diameter (mm)	0.25		Assumed
Bed porosity	0.39 (nano), 0.49 (micron)		Measured
Particle porosity	0.54 (nano), 0.49 (micron)		Measured
Heat capacity [$J/(K \cdot g)$]	1.27		Reference[50]
Carrier Gas			
Molecular weight ($g \cdot mol^{-1}$)	4.0		NIST
Heat capacity [$J/(K \cdot g)$]	5.19		NIST

Calculation of the MTZ was performed using equation (12):

$$1 - \left(\frac{time\ to\ breakthrough\ \left(\frac{C}{C0}>1\times10^{-4}\right), min}{time\ of\ bed\ saturation\ \left(\frac{C}{C0}=0.95\right), min} \right) \times bed\ length, cm \qquad (12)$$

Calculation of the CO_2/N_2 selectivity for the competitive dynamic adsorption experiments was performed using equation (13):

$$CO_2/N_2 \text{ Selectivity} = \left(\frac{q_{CO_2}}{n_{CO_2}}\right) \Big/ \left(\frac{q_{N_2}}{n_{N_2}}\right) \quad (13)$$

Where q is the differential loading of the adsorbate and n is the molar amount of adsorbate in the feed.

Results and Discussion

Synthesis and Characterisation of K-CHA

A conventional well-studied micron-sized K-CHA was prepared according to the patent literature of Bourgogne *et al*.[40, 51, 52] The nano-sized K-CHA was prepared following an up-scaled procedure derived from our previous work by Ghojavand *et al.* using an identical precursor composition, ageing time, and hydrothermal treatment.[42, 43] The synthesis of nano-sized chabazite has been methodically optimised to obtain discrete zeolite nano-crystallites of sizes below 100 nm with a specific Si/Al ratio. Both samples are highly crystalline (Fig. S4) with near-identical chemical compositions (Table S1); the XRD patterns of both samples are consistent with those previously reported for hydrated K-CHA.[53] The broad Bragg reflections of the nano-sized K-CHA are indicative of the presence of nano-sized crystalline domains.[42] The size of the crystalline domains was determined by Scherrer analysis as 80 nm for the nano-sized K-CHA and 200 nm for the micron-sized K-CHA. Thermogravimetric analysis of the nano- and micron-sized K-CHA samples reveals they possess a similar content of water of 17 and 19 wt% respectively (Fig. S5). Scanning electron microscopy (SEM) results confirms the order of magnitude difference in the particle size between the samples. Analysis of the nano-sized K-CHA shows the sample is composed of discrete nano-crystallites with primary particle sizes ranging predominantly between 50–80 nm (Figs S6a).[42] In comparison, the morphology of the micron-sized K-CHA is that of

294 irregular flake-like particles approximately 100–300 nm thick and 400–1000 nm at maximum
295 width; the particles are composed of intergrown crystallite aggregates approximately 40–80
296 nm in size (Figs S6b).[52]

297 The difference in the textural properties of both samples is also evidenced by N_2 sorption
298 analysis performed at −196 °C; both samples exhibit low micropore adsorption due to
299 trapdoor behaviour which restricts access of N_2 to the micropores, however, the nano-sized
300 K-CHA possesses significant inter-particle mesoporosity at high relative pressure due to its
301 nanoparticle morphology (Fig. S7).[40] Both samples were subjected to single component
302 CO_2 and N_2 sorption analysis at 20, 40 and 60 °C up to 1 bar (Figs 1 (a) and (b), Tables S2
303 and S3). The CO_2 and N_2 adsorption capacity decreases with increasing temperature (Fig. 1);
304 for both samples, the adsorbed amount of N_2 is low and increases linearly with increasing
305 pressure while CO_2 exhibits a Type I isotherm due to strong adsorbent-adsorbate interactions.
306 The slightly lower CO_2 adsorption capacity of the nano-sized K-CHA is due to the presence
307 of a phillipsite impurity. The isosteric enthalpy of adsorption (ΔH_{ads}) as a function of loading
308 were determined from the raw single-component isotherms (Fig. 1(c)). Both samples exhibit
309 near-homogeneous adsorption sites for CO_2; the ΔH_{ads} of the nano-sized K-CHA decreases
310 above a coverage of 2 mmol/g due to the saturation of the dual-cation adsorption sites and
311 limited inter-molecular interactions.[35, 43, 54, 55] Both samples also exhibit similar trends
312 for the N_2 ΔH_{ads} with a minor decrease as the loading increases, however, the decrease is
313 more significant for the nano-sized K-CHA. The lower N_2 ΔH_{ads} of the nano-sized K-CHA is
314 ascribed to the higher external surface of the particles providing lower energy adsorption
315 sites. Temperature-dependent modelling of the CO_2 adsorption isotherms was performed
316 using the Sips, Dual-Site Langmuir and Toth equations. The Toth model afforded the best
317 goodness of fit of the data (Fig. S8) and the parameters obtained were used for the modelling
318 of the CO_2 breakthrough curves (Table S4). Satisfactory temperature-dependent models of

the N_2 adsorption isotherms could not be obtained ($R^2 < 0.990$) and so the IAST selectivity was not determined.

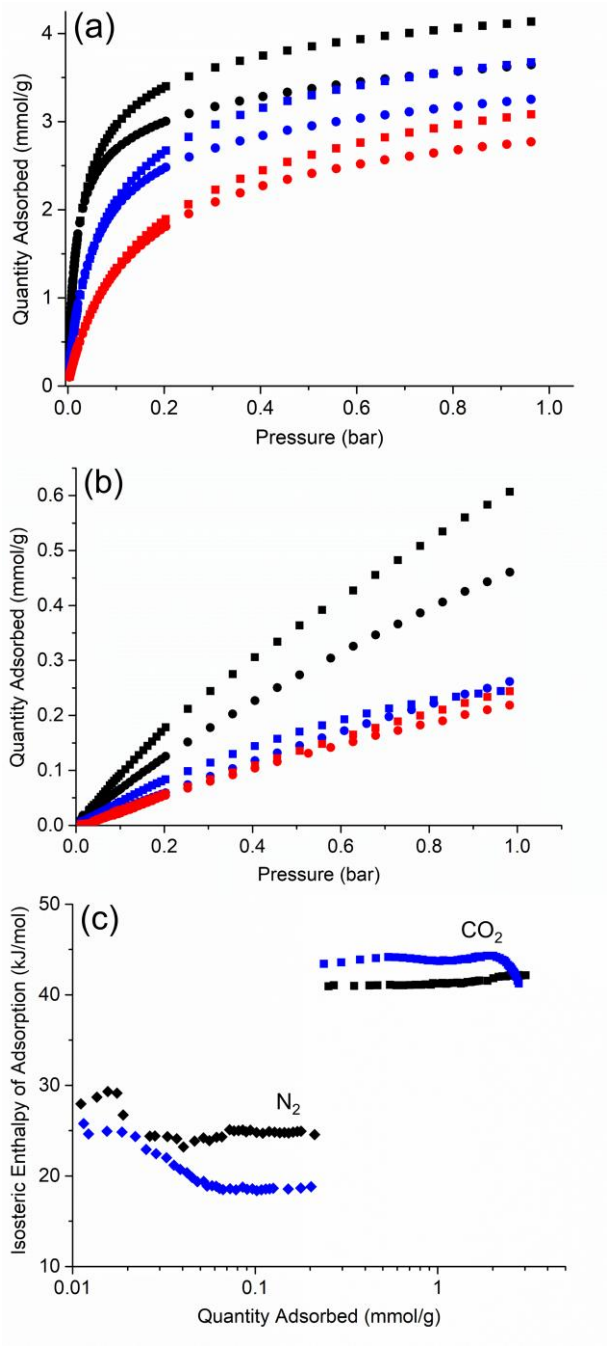

Figure 1. (a) CO_2 and (b) N_2 adsorption isotherms recorded at 20 (black), 40 (blue) and 60 °C (red) on nano-sized (circles) and micron-sized (squares) K-CHA. (c) CO_2 (squares) and N_2 (diamonds) isosteric enthalpies of adsorption for nano-sized (blue) and micron-sized (black) K-CHA.

Dynamic Adsorption of CO_2/N_2 on K-CHA and Breakthrough Curve Modelling

Breakthrough curve analysis of the K-CHA samples was conducted using a ternary mixture of $He/N_2/CO_2$ (70/25/5 vol%) at 1 bar and 20, 40 and 60 °C (Fig. 2); plots of the entire adsorption step show the breakthrough of N_2 on the K-CHA samples is instantaneous and exhibits a roll-up feature due to the displacement of N_2 by CO_2 from within the bed (Fig. S9). Due to the difference of the mass between the adsorbent, column and water bath the temperature profile of the column did not change significantly during the breakthrough experiment (Figure S10, Table S5). A minor temperature excursion of 0.30 and 0.25 °C was observed for the micron- and nano-sized K-CHA for the breakthrough curve analyses at 20 °C; smaller deviations were observed at 40 °C, and no discernible temperature excursion was observed at 60 °C. The CO_2 breakthrough profiles of the K-CHA samples clearly exhibit significantly steeper curves for the nano-sized K-CHA across the measured temperatures compared to the micron-sized sample (Fig. 2a), indicative of more uniform diffusion of CO_2 through the bed and a reduction in the length of the MTZ, *i.e.* enhanced overall kinetics. While both K-CHA samples were prepared with the same mesh, the discrete nano-crystallites of the nano-sized K-CHA facilitate significantly more rapid intraparticle diffusion. This is also visualised by the plots of $d(C/C_0)/dt$ illustrating the higher rate of change of the slope of the breakthrough curve for the nano-sized K-CHA compared to the micron-sized K-CHA (Figs 2c and d). A slight decrease in the slope of the breakthrough curve for nano-sized K-CHA occurs when the temperature increases from 20 to 40 °C, while the micron-sized K-CHA exhibits a slight increase in the breakthrough curve slope above 40 °C. The time necessary to achieve the desorption under pure He flow (Fig 2b) of CO_2 ($C/C_0 < 0.05$) dramatically decreased with increasing temperature for both samples; at 60 °C the nano- and micron-sized K-CHA required 11 and 14 minutes respectively. The difference in the desorption behaviour between the samples is not as dramatic as the initial breakthrough

because of the endothermic nature of the desorption step. Increasing the bed temperature from 20 to 60 °C resulted in a linear decrease of the differential loading of CO_2 at saturation for both K-CHA samples (Table 2). The differential loadings of CO_2 calculated from the competitive breakthrough curves compare well with the isotherm values. In comparison, the integration of the N_2 loading from the breakthrough curves affords values five times higher compared to the equilibrium isotherms. Alternatively, integration under the N_2 desorption curves was performed to calculate the N_2 loading, affording realistic values comparable to earlier work by Du *et al.*[56] Overall, both samples exhibit similar selectivity towards CO_2 over N_2; the nano-sized K-CHA exhibits slightly higher CO_2 loading under dynamic adsorption conditions.

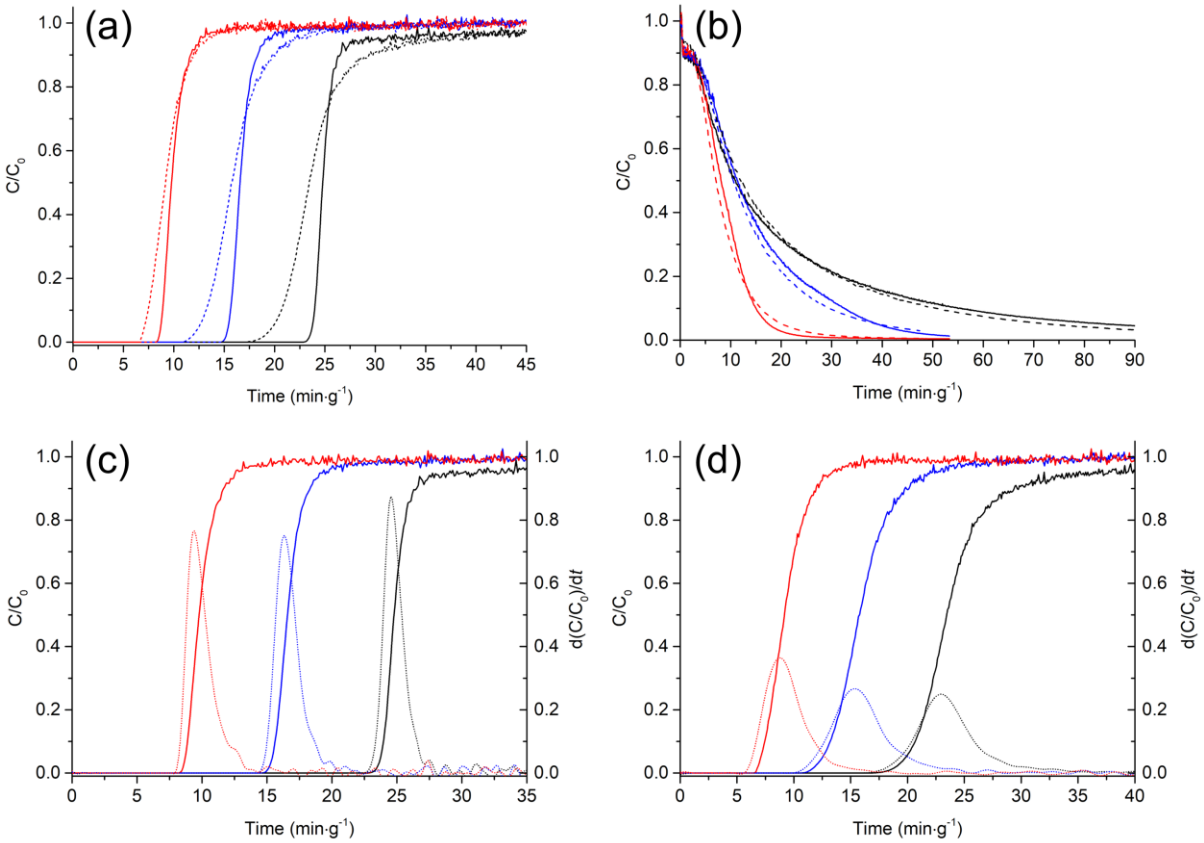

Figure 2. CO_2 breakthrough and desorption curves, and first derivatives of CO_2 breakthrough curves at 20 °C (black), 40 °C (blue) and 60 °C (red) obtained from competitive dynamic adsorption experiments, $He/N_2/CO_2$, 70/25/5. (a) CO_2 breakthrough curves and (b) CO_2 desorption curves of the nano-sized (solid) and micron-sized (dashed) K-CHA zeolites. CO_2 breakthrough curves (solid) and first derivative (dashed) of the (c) nano-sized and (d) micron-sized K-CHA zeolites.

Table 2. Differential loading of CO_2 calculated from breakthrough curves at saturation, N_2 differential loading calculated from desorption curves, and CO_2/N_2 selectivity calculated from equation 13. Data from breakthrough curve analysis ($He/N_2/CO_2$, 70/25/5) at 20, 40 and 60 °C.

Temperature (°C)	Nano-sized K-CHA			Micron-sized K-CHA		
	Differential loading, q (mmol/g)		CO_2/N_2 selectivity	Differential loading, q (mmol/g)		CO_2/N_2 selectivity
	CO_2	N_2		CO_2	N_2	
20	2.33	0.085	137	2.22	0.092	121
40	1.49	0.041	182	1.43	0.070	102
60	0.87	0.007	618	0.82	0.006	685

Comparison of the CO_2 breakthrough curves of the nano- and micron-sized K-CHA at 60 °C, akin to flue gas conditions, further highlights the difference in the performance of the solid adsorbents with different particle sizes (Fig. S11). By defining the MTZ between the first point of breakthrough, $C/C_0 > 1\times10^{-4}$ (*i.e.* the end of pure production of the weakly adsorbing component), and saturation of the bed, $C/C_0 = 0.95$, it is clear that the micron-sized K-CHA not only exhibits a shallower breakthrough curve but also takes a longer time to reach equilibrium. Due to the similar CO_2 uptakes of 0.87 mmol/g for both K-CHA samples at 0.05 bar (*i.e.* the partial pressure of CO_2 in the feed) at 60 °C, the longer time to reach equilibrium for the micron-sized K-CHA is ascribed to the larger particle size and thus longer diffusion path length. Expressed as a percentage of the total bed length, the length of the MTZ is significantly shorter (35% *vs* 52%) for the nano- compared to the micron-sized K-CHA (Table S6).

In addition, simple modelling of the CO_2 breakthrough curves was performed to extract the effective mass transfer coefficient, or linear driving force parameter (k_{LDF}), to describe the mass transfer kinetics of CO_2 through the adsorbent bed (Fig. 3).[44] Thus a global characteristic of the diffusion can be compared between the two samples. Employing the parameters derived from the Toth models of the CO_2 adsorption isotherms at different temperatures, the fitted model of the CO_2 breakthrough on the nano-sized K-CHA was found

to have 1–2 orders of magnitude higher k_{LDF} compared to that of the micron-sized K-CHA (Table 3), consistent with the sharper experimental breakthrough curves. The calculated CO_2 equilibrium loadings from the breakthrough curve modelling agree well with the experimental values, within 10% error. The k_{LDF} for CO_2 of the micron-sized K-CHA are of a similar magnitude to those of other commercial zeolite adsorbents such as NaX, CaA and 4A.[44, 57, 58] Modelling of the CO_2 breakthrough curves for the micron-sized K-CHA using the maximal loading term extracted from the isotherm modelling resulted in slight offsets between the experimental and modelled curves. This is may be due to the CO_2 equilibrium adsorption curves of the micron-sized K-CHA having not completely levelled off leading to an overestimation of the $q_{max,i}$.[59] To fit the model to the experimental data the maximal loading terms were reduced by 10%, 7% and 4% for the curves at 20 °C, 40 °C and 60 °C respectively. The adjustments to the maximal loading did not affect the k_{LDF} values of the fitted curves (Fig. S12).[60]

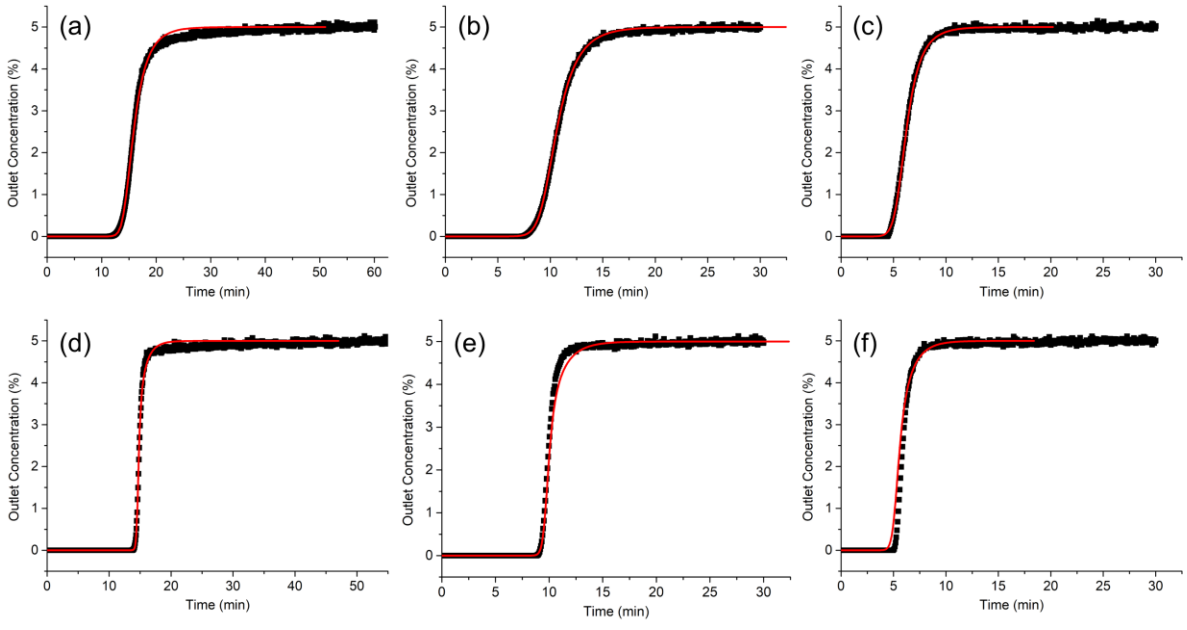

Figure 3. Experimental CO_2 breakthrough curves (black squares) and the fitted model of CO_2 breakthrough curves (red lines) using the parameters from Tables 1 and S4 for the micron-sized K-CHA at (a) 20 °C, (b) 40 °C and (c) 60 °C, and for the nano-sized K-CHA at (d) 20 °C, (e) 40 °C and (f) 60 °C.

Table 3. Calculated linear driving force parameters and CO_2 equilibrium loadings obtained from the modelling of the CO_2 breakthrough curves for the nano- and micron-sized K-CHA at 20, 40 and 60 °C.

Temperature (°C)	k_{LDF} (s^{-1})		CO_2 equilibrium loading (mmol/g)	
	Nano-sized K-CHA	Micron-sized K-CHA	Nano-sized K-CHA	Micron-sized K-CHA
20	2.37	0.0221	2.35	2.26
40	2.93	0.0442	1.61	1.51
60	3.27	0.125	0.92	0.90

To better understand the effect of particle size on the performance and diffusion properties of the K-CHA samples, mercury porosimetry analysis of the meshed K-CHA samples was performed, and diffusion resistances were considered using established correlations in the literature.[46, 61] Plots of the pore diameter against the cumulative pore volume (Fig. 4a) and pore size distribution (Fig. 4b) of the meshed K-CHA samples reveal two intrusion events corresponding to the initial filling of the macropores (interparticle porosity) and the filling of the remaining macropores and mesopores. Both samples exhibit similar intrusion of the interparticle porosity, however, the distribution of the macropores is different. The majority (80%) of the macropore volume of the meshed nano-sized K-CHA occurs for pores ≥6 μm while for the meshed micron-sized K-CHA this corresponds to 61% (Table S7). This may be ascribed to the more uniform morphology of the nano-sized K-CHA compared to the flake-like morphology of the micron-sized K-CHA. The filling of the mesopores (7–50 nm) shows that the meshed nano-sized K-CHA exhibits ≈14 times higher mesopore volume compared to the meshed micron-sized K-CHA. This is a clear result of the meshed particle being composed of smaller discrete nanocrystals. For the nano-sized K-CHA the mesopores account for approximately 17% of the total pore volume determined by Hg porosimetry, while for the micron-sized K-CHA this value is 1.3%.

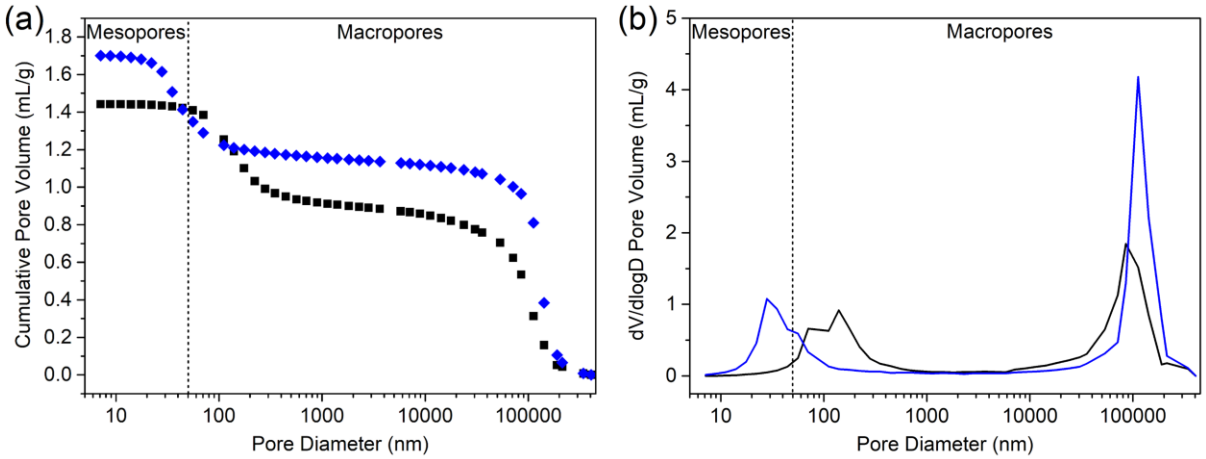

Figure 4. Plot of the pore diameter (nm) *vs* the (a) cumulative pore volume, and (b) pore size distribution for the meshed nano-sized (blue) and micron-sized (black) K-CHA zeolite.

Considering that each of the eight-membered ring pore apertures of K-CHA are occupied by extra-framework K^+ cations and are comparable in size to CO_2, like for 4A zeolite, it may be expected that the diffusion behaviour of K-CHA to be micropore controlled.[62] However, considering that the meshed particle sizes are 0.25–0.5 mm, axial dispersion may be expected to contribute significantly to the mass transfer behaviour.[63] Recent breakthrough curve analysis of N_2/O_2 on lithium exchanged low silica X (LiLSX) zeolite demonstrated that axial dispersion effects must be considered for small particles and at low Reynolds number which is the case in this work.[64] The contributions from the different diffusion resistances to the overall mass transfer coefficient k_i were calculated using equation (14), which is a generalisation of the Glueckauf approximation[46]:

$$\frac{1}{k_i} = \frac{Kr_p}{3k_f} + \frac{Kr_p^2}{15\varepsilon_p D_p} + \frac{r_c^2}{15D_c} \quad (14)$$

where the first, second and third terms on the right-hand side of equation 14 represent the film mass transfer, macropore, and micropore resistances, and K is the equilibrium Henry's law constant. Calculation of the values for the axial dispersion, film and macropore contributions were performed using established correlations and experimental data.[46, 61]

451 However, due to the unavailability of experimental intracrystalline diffusivity values for CO_2
452 in high-aluminium cation-containing chabazite zeolites, the micropore contribution was
453 estimated by subtracting the film and macropore contributions from the effective mass
454 transfer coefficients extracted from the breakthrough curve modelling. The calculated
455 intracrystalline diffusivity values of CO_2 for the K-CHA zeolites are 3–4 orders of magnitude
456 greater than for 4A.[65] Details describing the calculation of each contribution are provided
457 in the supporting information; the values and percentages of k_i are presented in Tables S12–
458 14. The calculations reveal that between the film, macropore and micropore resistances, the
459 micropore contribution is the most significant, being several orders of magnitude greater and
460 accounting for >99.5% of the mass transfer coefficient for the micron-sized K-CHA across all
461 measured temperatures. For the nano-sized K-CHA the micropore resistance is much less
462 significant than for the micron-sized K-CHA, but still accounts for 83, 87 and 92% of the
463 mass transfer coefficient at 20, 40 and 60 °C respectively. Both samples exhibit similar
464 absolute values of film and macropore resistance; their relative contribution is more
465 significant for the nano-sized K-CHA. Both K-CHA samples exhibit similar absolute values
466 for the contribution of axial dispersion, which are similar or greater in value to the
467 contribution of the micropore resistance. For the micron-sized K-CHA, the ratio of the axial
468 dispersion to micropore resistance increases from 0.8 at 20 °C to 1.1 at 40 °C and 2.1 at 60
469 °C due to the greater decrease in the micropore resistance. For the nano-sized K-CHA, the
470 ratio of the axial dispersion to the micropore resistance is significantly higher (54–91). This
471 indicates that the mass transfer behaviour of the meshed nano-sized K-CHA is primarily
472 affected by axial dispersion; the ratio of the axial dispersion to the micropore resistance
473 decreases with increasing temperature.

474 For comparison, the contributions from the lumped resistances and axial dispersion were also
475 explored by varying either the k_{LDF} parameter or axial dispersion values for the modelling of

476 the breakthrough curves.[58] Consistent with the trend of the calculated values presented in
477 Table S12 the shape of the modelled CO_2 breakthrough curves for the nano-sized K-CHA are
478 susceptible to variations in the axial dispersion, while varying the k_{LDF} parameter results in
479 little change (Fig S13). In comparison, the micron-sized K-CHA is much more susceptible to
480 changes of the k_{LDF} parameter, and similarly susceptible to changes of the axial dispersion
481 (Fig. S14). While increased axial dispersion increases spreading of the MTZ, the
482 experimental results presented here indicate that for adsorbent particles of identical size and
483 composition, reducing the size of the discrete crystals within the meshed particle may reduce
484 the size of the MTZ. Analysis of the results indicate this is primarily attributed to the
485 reduction of the micropore resistance, which may be a consequence of the shorter
486 intracrystalline diffusion pathway of CO_2 within the nano-sized K-CHA. While the
487 introduction of mesoporosity has shown to improve the CO_2 adsorption kinetics for LTA
488 zeolite, in the present case where the nano-sized K-CHA exhibits an order of magnitude
489 greater mesopore volume than the micron-sized K-CHA, the contribution from the macropore
490 diffusion resistance is negligible.[66]

491 Multiple cycles of CO_2 breakthrough, and desorption under pure He at 60 °C also
492 demonstrates the improved performance of the nano-sized K-CHA (Fig. 5) which exhibits a
493 29% higher CO_2 differential loading for the first cycle (Table 4). The CO_2 loading was
494 calculated up to the first point of breakthrough. Upon subsequent cycles of CO_2 adsorption,
495 and desorption under pure He, the CO_2 capacities of both samples decreases due to the
496 formation of chemisorbed carbonate species and the incomplete removal of adsorbed CO_2 by
497 He during the desorption step.[43] This is supported by integration of the CO_2 desorption
498 curves for the nano and micron-sized K-CHA at 60 °C which afforded 0.76 and 0.73 mmol/g,
499 or 87 and 88% of the differential loadings at saturation (Table 2). Over the next three cycles,
500 on average, the nano-sized K-CHA exhibits better performance up to the end of pure

production of the weakly adsorbing component, losing only 14% of its initial CO_2 capacity while the micron-sized K-CHA loses approximately 29% (Table 4). This may be due to compositional inhomogeneity of the micron-sized K-CHA particles due to their preparation by interzeolite conversion and the different solubilities of Si and Al species, as well as the possibility of internal structural rearrangements due to the long hydrothermal treatment time (15 days).[67] This rationale is supported by comparing the relative amounts of CO_2 chemisorbed species. *In situ* FTIR spectroscopic analysis of the micron-sized K-CHA in the presence of CO_2 (17.9 kPa) revealed ~3 times greater the amount of CO_2 chemisorbed species compared to nano-sized K-CHA, *i.e.* 5% *vs* 1.7% of the total physisorbed and chemisorbed CO_2 (Fig. S15).[43]

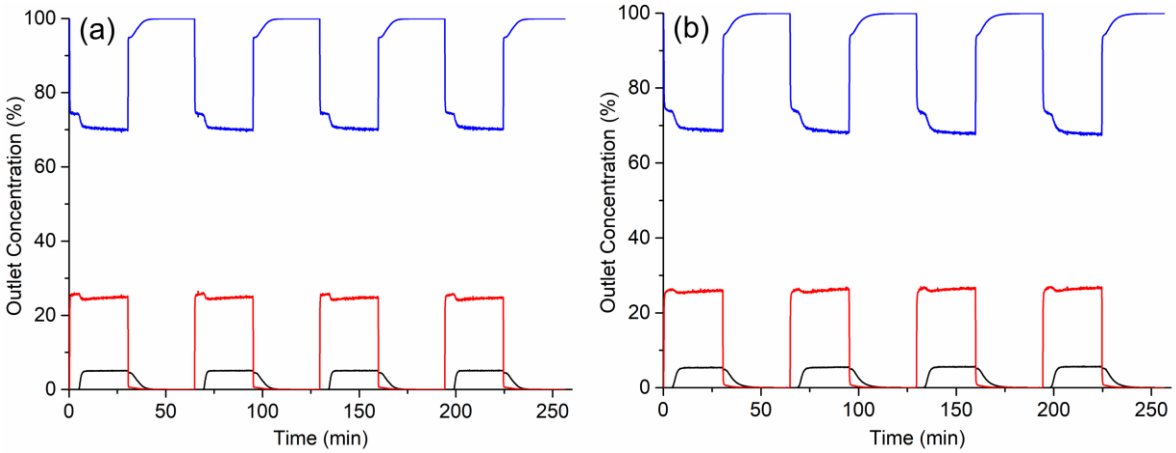

Figure 5. Four consecutive cycles of the adsorption step ($He/N_2/CO_2$, 70/25/5) and desorption step (He, 100) for breakthrough curve analysis on the (a) nano-sized K-CHA and (b) micron-sized K-CHA at 60 °C. Colour legend: He (blue), N_2 (red), and CO_2 (black).

Table 4. Differential loading of CO_2 calculated from CO_2 breakthrough curves at $C/C_0 > 1\times10^{-4}$ on nano- and micron-sized K-CHA subjected to multiple cycles of breakthrough ($He/N_2/CO_2$, 70/25/5) and desorption (He, 100) at 60 °C.

Cycle	CO_2 differential loading, q (mmol/g)	
	Nano-sized K-CHA	Micron-sized K-CHA
1	0.66	0.51
2	0.56	0.35
3	0.56	0.36
4	0.57	0.36

In situ FTIR Analysis of the Silanol Environments

To consider the role defects may play in the separation performance of the K-CHA samples, *in situ* FTIR spectroscopic analysis was also employed to examine the distributions of silanol environments on both K-CHA samples (Fig. 6). Analysis before and after breakthrough curve experiments reveals two peaks at 3740 cm^{-1} and 3727 cm^{-1} attributed to isolated silanol sites corresponding to the external surfaces of the different K-CHA samples.[68] These peaks are significantly more intense for the nano-sized K-CHA due to its larger external surface area. Both micron and nano-sized K-CHA samples show a broad complex band in the range of 3333 and 3668 cm^{-1}. These peaks can be attributed to the internal silanol sites exhibiting strong hydrogen bonding between them.[68] The micron-sized K-CHA exhibits a greater initial population (black trace) of strong internal hydrogen bonding sites which may reflect internal framework T-atom vacancies or missing T–O–T bonds due to the intergrown nature of the crystallites. After multiple pre-treatment and breakthrough cycles this band decreases slightly (grey trace). Conversely, the nano-sized K-CHA exhibits fewer sites initially (navy trace) and an increased population of these sites after multiple pre-treatment and breakthrough cycles (blue trace). This suggests that despite an increase in the population of strong hydrogen-bonding silanol sites on the nano-sized K-CHA the diffusion performance is dominated by the effect of the particle size difference. Deconvolution and exact peak assignment in this region is not possible using exclusively FTIR spectroscopy and requires additional characterization techniques (*i.e.* ^{1}H MAS NMR) beyond the scope of this work. Table 5 presents the concentration of the silanol sites obtained by integration of the silanol region for both the nano- and micron-sized K-CHA samples before and after the breakthrough measurements. For both the nano- and micron-sized K-CHA samples a reduction of ~27% of the silanol sites are observed after the breakthrough measurements

(Table 5). This can be partly attributed to the residual chemisorbed species chemically bonded to the silanol sites and in agreement with our previous work.[43]

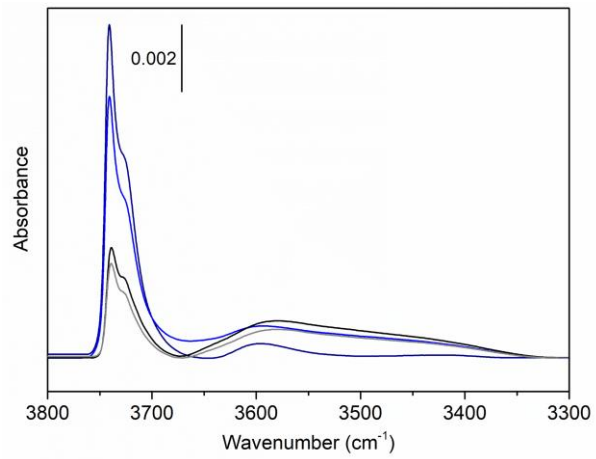

Figure 6. *In situ* FTIR spectra at 25 °C highlighting the silanol region of the nano-sized (navy, blue) and micron-sized (black, grey) K-CHA samples zeolite (before, after breakthrough curve analysis). Samples were pre-treated at 300 °C under high vacuum (10^{-6} kPa) prior to measurement.

Table 5. The concentration of silanol sites of micron and nano-sized K-CHA samples before (fresh) and after (used) breakthrough measurements obtained using *in situ* FTIR spectroscopy.

Sample		**Silanol site concentration ($cm^{-1} \cdot g^{-1}$)**
Nano-sized K-CHA	Fresh	403
	Used	288
Micron-sized K-CHA	Fresh	306
	Used	224

Conclusions

As we move towards the need to control process rate, by improving the diffusion properties of zeolites through the organic-template free direct synthesis of discrete zeolite nanoparticles, instead of employing post-synthetic treatments, significant enhancements in the separation performance can be achieved. By comparing meshed micron-sized and nano-sized K-CHA with identical Si/Al ratios and cation compositions for CO_2 separation from N_2, the diffusion of CO_2 through the bed of meshed nano-sized K-CHA is more rapid and uniform.

Breakthrough curve analysis shows steeper breakthrough curves and more rapid achievement of equilibrium for the meshed nano-sized K-CHA due to the smaller discrete particle size. While textural analysis by Hg porosimetry reveals improved mesoporosity for the nano-sized K-CHA, back-calculation of the diffusion coefficients reveals significantly lower micropore diffusion resistance as responsible for the improved mass transfer behaviour. This translates to a greater k_{LDF} of the modelled and fitted CO_2 breakthrough curves and a reduction in the size of the MTZ by 17% despite the significant contribution from axial dispersion to the mass transfer behaviour. Furthermore, we also observe that the nano-sized K-CHA has approximately three times less CO_2 chemisorbed species than micron-sized K-CHA. When scouting for improved adsorbents, most academic researchers often concentrate on capacity and selectivity and pay less attention to the kinetics of the process. The combination of these three features will determine the productivity, often referred to in catalysis as STY (space time yield, units: moles of a desired product.time^{-1}·reactor volume^{-1}). STY is a key parameter to design the size of a unit, *i.e.*, this investment cost (CAPEX). While these results support the potential of nanozeolites in realising greater performance improvements, further investigation of the diffusion behaviour of nanozeolites in larger columns and their comparison to micron-sized counterparts will yield greater insights due to the variety of pore sizes, framework topologies, elemental compositions and shaping factors of zeolites which influence the diffusion properties.

Declaration of Competing Interests

The authors declare no competing financial or professional interests.

Acknowledgements

E. B. C. would like to thank Carsten Blum and Sebastian Ehrling for their helpful discussions, and Izabel Medeiros-Costa for her help with mercury porosimetry. This project

has received funding from the Region of Normandy via the Label of Excellence for the Centre of Zeolites and Nanoporous Materials and the Industrial Chair Project "ECOGAS" supported by the Region of Normandy and TotalEnergies.

References

[1] S. Sircar, A.L. Myers, Gas Separation by Zeolites, in: S.M. Auerbach, K.A. Carrado, P.K. Dutta (Eds.) Handbook of Zeolite Science and Technology, Marcel Dekker, Inc., New York, Basel, 2003, pp. 1063-1104.
[2] Y.S. Bae, R.Q. Snurr, Development and evaluation of porous materials for carbon dioxide separation and capture, Angew. Chem. Int. Ed., 50 (2011) 11586-11596.
[3] A. Samanta, A. Zhao, G.K. Shimizu, P. Sarkar, R. Gupta, Post-combustion CO_2 capture using solid sorbents: a review, Ind. Eng. Chem. Res., 51 (2012) 1438-1463.
[4] B. Li, Y. Duan, D. Luebke, B. Morreale, Advances in CO_2 capture technology: A patent review, Appl. Energy, 102 (2013) 1439-1447.
[5] D.Y. Leung, G. Caramanna, M.M. Maroto-Valer, An overview of current status of carbon dioxide capture and storage technologies, Renew. Sust. Energ. Rev., 39 (2014) 426-443.
[6] O. Cheung, N. Hedin, Zeolites and related sorbents with narrow pores for CO_2 separation from flue gas, RSC Adv., 4 (2014) 14480-14494.
[7] M. Pera-Titus, Porous inorganic membranes for CO_2 capture: present and prospects, Chem. Rev., 114 (2014) 1413-1492.
[8] P.A. Webley, Adsorption technology for CO_2 separation and capture: a perspective, Adsorption, 20 (2014) 225-231.
[9] N. Gargiulo, F. Pepe, D. Caputo, CO_2 adsorption by functionalized nanoporous materials: a review, J. Nanosci. Nanotechnol., 14 (2014) 1811-1822.
[10] S.-Y. Lee, S.-J. Park, A review on solid adsorbents for carbon dioxide capture, J. Ind. Eng. Chem., 23 (2015) 1-11.
[11] N. Kosinov, J. Gascon, F. Kapteijn, E.J. Hensen, Recent developments in zeolite membranes for gas separation, J. Membr. Sci., 499 (2016) 65-79.
[12] E.S. Sanz-Perez, C.R. Murdock, S.A. Didas, C.W. Jones, Direct capture of CO_2 from ambient air, Chem. Rev., 116 (2016) 11840-11876.
[13] M. Younas, M. Sohail, L. Leong, M. Bashir, S. Sumathi, Feasibility of CO_2 adsorption by solid adsorbents: a review on low-temperature systems, Int. J. Environ. Sci. Technol., 13 (2016) 1839-1860.
[14] H.A. Patel, J. Byun, C.T. Yavuz, Carbon dioxide capture adsorbents: chemistry and methods, ChemSusChem, 10 (2017) 1303-1317.
[15] M. Vinoba, M. Bhagiyalakshmi, Y. Alqaheem, A.A. Alomair, A. Pérez, M.S. Rana, Recent progress of fillers in mixed matrix membranes for CO_2 separation: A review, Sep. Purif. Technol., 188 (2017) 431-450.
[16] M. Abu Ghalia, Y. Dahman, Development and evaluation of zeolites and metal–organic frameworks for carbon dioxide separation and capture, Energy Technol., 5 (2017) 356-372.
[17] M. Oschatz, M. Antonietti, A search for selectivity to enable CO_2 capture with porous adsorbents, Energy Environ. Sci., 11 (2018) 57-70.
[18] Y. Han, Z. Zhang, Nanostructured membrane materials for CO_2 capture: a critical review, J. Nanosci. Nanotechnol., 19 (2019) 3173-3179.

[19] S. Kumar, R. Srivastava, J. Koh, Utilization of zeolites as CO2 capturing agents: Advances and future perspectives, J. CO2 Util., 41 (2020) 101251.
[20] S.C. Peter, B. Ray, S.R. Churipard, An overview of the materials and methodologies for CO_2 capture under humid conditions, J. Mater. Chem. A, 9 (2021) 26498-26527.
[21] A.H. Farmahini, S. Krishnamurthy, D. Friedrich, S. Brandani, L. Sarkisov, Performance-based screening of porous materials for carbon capture, Chem. Rev., 121 (2021) 10666-10741.
[22] R.S. Liu, X.D. Shi, C.T. Wang, Y.Z. Gao, S. Xu, G.P. Hao, S. Chen, A.H. Lu, Advances in post- combustion CO_2 capture by physical adsorption: from materials innovation to separation practice, ChemSusChem, 14 (2021) 1428-1471.
[23] F.G. Kerry, Industrial Gas Handbook: Gas Separation and Purification, CRC press, Boca Raton, FL, 2007.
[24] Z. Zhang, T.N. Borhani, A.G. Olabi, Status and perspective of CO_2 absorption process, Energy, 205 (2020) 118057.
[25] F. Raganati, F. Miccio, P. Ammendola, Adsorption of carbon dioxide for post-combustion capture: a review, Energy Fuels, 35 (2021) 12845-12868.
[26] R.L. Siegelman, E.J. Kim, J.R. Long, Porous materials for carbon dioxide separations, Nat. Mater., 20 (2021) 1060-1072.
[27] P. Hovington, O. Ghaffari-Nik, L. Mariac, A. Liu, B. Henkel, S. Marx, Rapid cycle temperature swing adsorption process using solid structured sorbent for CO_2 capture from cement flue gas, Proceedings of the 15th Greenhouse Gas Control Technologies Conference, Abu Dhabi, UAE, 2021, pp. 15-18.
[28] W. Vermeiren, J.-P. Gilson, Impact of Zeolites on the Petroleum and Petrochemical Industry, Top. Catal., 52 (2009) 1131-1161.
[29] P. Peng, D. Stosic, X.-M. Liu, Z.-F. Yan, S. Mintova, Strategy towards enhanced performance of zeolite catalysts: raising effective diffusion coefficient versus reducing diffusion length, Chem. Eng. J., 385 (2020) 123800.
[30] P. Peng, D. Stosic, A. Aitblal, A. Vimont, P. Bazin, X.-M. Liu, Z.-F. Yan, S. Mintova, A. Travert, Unraveling the diffusion properties of zeolite-based multicomponent catalyst by combined gravimetric analysis and IR spectroscopy (AGIR), ACS Catal., 10 (2020) 6822-6830.
[31] D. Kerstens, B. Smeyers, J. Van Waeyenberg, Q. Zhang, J. Yu, B.F. Sels, State of the art and perspectives of hierarchical zeolites: practical overview of synthesis methods and use in catalysis, Adv. Mater., 32 (2020) 2004690.
[32] E.-P. Ng, D. Chateigner, T. Bein, V. Valtchev, S. Mintova, Capturing ultrasmall EMT zeolite from template-free systems, Science, 335 (2012) 70-73.
[33] H. Awala, J.-P. Gilson, R. Retoux, P. Boullay, J.-M. Goupil, V. Valtchev, S. Mintova, Template-free nanosized faujasite-type zeolites, Nat. Mater., 14 (2015) 447-451.
[34] J. Grand, N. Barrier, M. Debost, E.B. Clatworthy, F. Laine, P. Boullay, N. Nesterenko, J.-P. Dath, J.-P. Gilson, S. Mintova, Flexible Template-Free RHO Nanosized Zeolite for Selective CO_2 Adsorption, Chem. Mater., 32 (2020) 5985-5993.
[35] M. Debost, P.B. Klar, N. Barrier, E.B. Clatworthy, J. Grand, F. Lainé, P. Brazda, L. Palatinus, N. Nesterenko, P. Boullay, S. Mintova, Synthesis of discrete CHA zeolite nanocrystals without organic templates for selective CO_2 capture, Angew. Chem. Int. Ed., 59 (2020) 23491-23495.
[36] E.B. Clatworthy, M. Debost, N. Barrier, S.p. Gascoin, P. Boullay, A.l. Vicente, J.-P. Gilson, J.-P. Dath, N. Nesterenko, S. Mintova, Room-Temperature Synthesis of BPH Zeolite Nanosheets Free of Organic Template with Enhanced Stability for Gas Separations, ACS Appl. Nano Mater, 4 (2020) 24-28.

[37] E.B. Clatworthy, A.A. Paecklar, E. Dib, M. Debost, N. Barrier, P. Boullay, J.-P. Gilson, N. Nesterenko, S. Mintova, Engineering RHO Nanozeolite: Controlling the Particle Morphology, Al and Cation Content, Stability, and Flexibility, ACS Appl. Energy Mater., 5 (2022) 6032-6042.
[38] M. Debost, E.B. Clatworthy, J. Grand, N. Barrier, N. Nesterenko, J.-P. Gilson, P. Boullay, S. Mintova, Direct synthesis of nanosized CHA zeolite free of organic template by a combination of cations as structure directing agents, Microporous Mesoporous Mater., (2022) 112337.
[39] K.C. Omehia, A.G. Clements, S. Michailos, K.J. Hughes, D.B. Ingham, M. Pourkashanian, Techno- economic assessment on the fuel flexibility of a commercial scale combined cycle gas turbine integrated with a CO_2 capture plant, Int. J. Energy Res., 44 (2020) 9127-9140.
[40] J. Shang, G. Li, R. Singh, Q. Gu, K.M. Nairn, T.J. Bastow, N. Medhekar, C.M. Doherty, A.J. Hill, J.Z. Liu, P.A. Webley, Discriminative separation of gases by a "molecular trapdoor" mechanism in chabazite zeolites, J. Am. Chem. Soc., 134 (2012) 19246-19253.
[41] F.N. Ridha, P.A. Webley, Anomalous Henry's law behavior of nitrogen and carbon dioxide adsorption on alkali-exchanged chabazite zeolites, Sep. Purif. Technol., 67 (2009) 336-343.
[42] S. Ghojavand, E.B. Clatworthy, A. Vicente, E. Dib, V. Ruaux, M. Debost, J. El Fallah, S. Mintova, The role of mixed alkali metal cations on the formation of nanosized CHA zeolite from colloidal precursor suspension, J. Colloid Interface Sci., 604 (2021) 350-357.
[43] S. Ghojavand, B. Coasne, E.B. Clatworthy, R. Guillet-Nicolas, P. Bazin, M. Desmurs, L. Jacobo Aguilera, V. Ruaux, S. Mintova, Alkali Metal Cations Influence the CO_2 Adsorption Capacity of Nanosized Chabazite: Modeling vs Experiment, ACS Appl. Nano Mater, 5 (2022) 5578-5588.
[44] A. Möller, R. Eschrich, C. Reichenbach, J. Guderian, M. Lange, J. Möllmer, Dynamic and equilibrium-based investigations of CO_2-removal from CH_4-rich gas mixtures on microporous adsorbents, Adsorption, 23 (2017) 197-209.
[45] N.S. Wilkins, A. Rajendran, Measurement of competitive CO_2 and N_2 adsorption on Zeolite 13X for post-combustion CO_2 capture, Adsorption, 25 (2019) 115-133.
[46] D.M. Ruthven, Principles of Adsorption and Adsorption Processes, Wiley, New York, 1984.
[47] W. Kast, Adsorption aus der Gasphase. Ingenieurwissenschaftliche Grundlagen und technische Verfahren, VCH, Weinheim, Germany, 1988.
[48] D.B. Bathen, M, Adsorptionstechnik, Springer, Berlin, 2001.
[49] E. Glueckauf, Theory of chromatography. Part 10.—Formulæ for diffusion into spheres and their application to chromatography, Trans. Faraday Society, 51 (1955) 1540-1551.
[50] A. Findikakis, Heat Capacity Analysis Report, Yucca Mountain Project, Las Vegas, NV (United States)2004.
[51] M. Bourgogne, J.-L. Guth, R. Wey, Process for the preparation of synthetic zeolites, and zeolites obtained by said process, Compagnie Francaise de Raffinage1985.
[52] S.-H. Hong, M.-S. Jang, S.J. Cho, W.-S. Ahn, Chabazite and zeolite 13X for CO_2 capture under high pressure and moderate temperature conditions, Chem. Commun., 50 (2014) 4927-4930.
[53] M. Calligaris, G. Nardin, L. Randaccio, Cation site location in hydrated chabazites. Crystal structure of potassium-and silver-exchanged chabazites, Zeolites, 3 (1983) 205-208.
[54] J. Zhang, R. Singh, P.A. Webley, Alkali and alkaline-earth cation exchanged chabazite zeolites for adsorption based CO_2 capture, Microporous Mesoporous Mater., 111 (2008) 478-487.

[55] T.D. Pham, M.R. Hudson, C.M. Brown, R.F. Lobo, Molecular basis for the high CO_2 adsorption capacity of chabazite zeolites, ChemSusChem, 7 (2014) 3031-3038.
[56] T. Du, X. Fang, L. Liu, J. Shang, B. Zhang, Y. Wei, H. Gong, S. Rahman, E.F. May, P.A. Webley, An optimal trapdoor zeolite for exclusive admission of CO_2 at industrial carbon capture operating temperatures, Chem. Commun., 54 (2018) 3134-3137.
[57] H. Yi, H. Deng, X. Tang, Q. Yu, X. Zhou, H. Liu, Adsorption equilibrium and kinetics for SO_2, NO, CO_2 on zeolites FAU and LTA, J. Hazard. Mater., 203 (2012) 111-117.
[58] L.F. Zafanelli, A. Henrique, M. Karimi, A.E. Rodrigues, J.A. Silva, Single- and Multicomponent Fixed Bed Adsorption of CO_2, CH_4, and N_2 in Binder-Free Beads of 4A Zeolite, Ind. Eng. Chem. Res., 59 (2020) 13724-13734.
[59] Q.H. Dirar, K.F. Loughlin, Intrinsic adsorption properties of CO_2 on 5A and 13X zeolite, Adsorption, 19 (2013) 1149-1163.
[60] J.C. Knox, A.D. Ebner, M.D. LeVan, R.F. Coker, J.A. Ritter, Limitations of breakthrough curve analysis in fixed-bed adsorption, Ind. Eng. Chem. Res., 55 (2016) 4734-4748.
[61] N.S. Wilkins, A. Rajendran, S. Farooq, Dynamic column breakthrough experiments for measurement of adsorption equilibrium and kinetics, Adsorption, 27 (2021) 397-422.
[62] D.M. Ruthven, Diffusion in type A zeolites: New insights from old data, Microporous Mesoporous Mater., 162 (2012) 69-79.
[63] M. Suzuki, J. Smith, Axial dispersion in beds of small particles, The Chemical Engineering Journal, 3 (1972) 256-264.
[64] A. Moran, M. Patel, O. Talu, Axial dispersion effects with small diameter adsorbent particles, Adsorption, 24 (2018) 333-344.
[65] H. Yucel, D.M. Ruthven, Diffusion of CO_2 in 4A and 5A zeolite crystals, J. Colloid Interface Sci., 74 (1980) 186-195.
[66] C. Chen, W.-S. Ahn, CO_2 adsorption on LTA zeolites: Effect of mesoporosity, Appl. Surf. Sci., 311 (2014) 107-109.
[67] J. Devos, M.A. Shah, M. Dusselier, On the key role of aluminium and other heteroatoms during interzeolite conversion synthesis, RSC Adv., 11 (2021) 26188-26210.
[68] E. Dib, I.M. Costa, G.N. Vayssilov, H.A. Aleksandrov, S. Mintova, Complex H-bonded silanol network in zeolites revealed by IR and NMR spectroscopy combined with DFT calculations, J. Mater. Chem. A, 9 (2021) 27347-27352.